

This copy is for your personal, non-commercial use only.

If you wish to distribute this article to others, you can order high-quality copies for your colleagues, clients, or customers by [clicking here](#).

Permission to republish or repurpose articles or portions of articles can be obtained by following the guidelines [here](#).

The following resources related to this article are available online at www.sciencemag.org (this information is current as of February 2, 2010):

Updated information and services, including high-resolution figures, can be found in the online version of this article at:

<http://www.sciencemag.org/cgi/content/full/322/5905/1243>

Supporting Online Material can be found at:

<http://www.sciencemag.org/cgi/content/full/1161820/DC1>

A list of selected additional articles on the Science Web sites **related to this article** can be found at:

<http://www.sciencemag.org/cgi/content/full/322/5905/1243#related-content>

This article **cites 24 articles**, 9 of which can be accessed for free:

<http://www.sciencemag.org/cgi/content/full/322/5905/1243#otherarticles>

This article has been **cited by** 5 article(s) on the ISI Web of Science.

This article has been **cited by** 3 articles hosted by HighWire Press; see:

<http://www.sciencemag.org/cgi/content/full/322/5905/1243#otherarticles>

This article appears in the following **subject collections**:

Cell Biology

http://www.sciencemag.org/cgi/collection/cell_biol

ditionally, no influence of SR alleles on female remating behavior has been shown (15). Third, we doubt that the remating rate increase was driven by SR populations being more inbred and females avoiding inbreeding depression (10), because our experimental populations of 120 adults per generation were large enough to avoid appreciable inbreeding (19). There also was no a priori reason to expect a greater inbreeding effect in the female-biased SR populations compared to the non-SR female-biased populations.

The most parsimonious explanation for the evolution of increased female remating rates in the presence of SR is therefore that the direct benefits of decreased risk of sperm limitation due to mating with SR males, combined with the benefit of reduced exposure of the progeny of polyandrous females to SR, has driven the spread of alleles for increased remating rates through the populations. The observed increases in female remating rates (2.75 versus 3.25 days) are well within the natural variation of the source population (2 to 5 days). Thus, we conclude that increased female remating rates evolved through selection for alleles that promote polyandry in SR populations.

Avoidance of selfish genetic elements is likely to promote the evolution of polyandry, wherever a selfish genetic element reduces both the sperm competitive ability of carrier males and the fitness of progeny that inherit the gene (7, 12). Sex chromosome meiotic drive elements are likely to considerably reduce male fertility

because their transmission mode involves a substantial failure of spermatogenesis (13, 14). They also impose serious costs because they destroy sperm and distort brood sex ratios (14). Sex chromosome drive is widespread (20) and may be common (21, 22). Most segregation distorters are active in males (23), and reduced sperm production associated with both X- and Y-chromosome drive has been observed (13). Similarly, males may suffer reduced fertility from other selfish genes, such as autosomal drive genes, B chromosomes (24), intracellular parasites (25), and possibly some transposons (26). Thus, a wide range of selfish genetic elements potentially provide the critical combination of low sperm competitive ability and low fitness that could favor polyandry. Because such selfish elements are ubiquitous in living organisms and frequently compromise male fertility, they may provide a generally overlooked explanation for why polyandry is very widespread.

References and Notes

1. T. R. Birkhead, A. P. Møller, *Sperm Competition and Sexual Selection* (Academic Press, London, 1998).
2. L. W. Simmons, *Sperm Competition and Its Evolutionary Consequences in the Insects* (Princeton Univ. Press, Princeton, NJ, 2001).
3. G. Arnqvist, L. Rowe, *Sexual Conflict* (Princeton Univ. Press, Princeton, NJ, 2005).
4. T. Chapman, L. F. Liddle, J. M. Kalb, M. F. Wolfner, L. Partridge, *Nature* **373**, 241 (1995).
5. H. Crudgington, M. Siva-Jothy, *Nature* **407**, 855 (2000).
6. M. D. Jennions, M. Petri, *Biol. Rev. Camb. Philos. Soc.* **75**, 21 (2000).

7. J. A. Zeh, D. W. Zeh, *Proc. R. Soc. London Ser. B* **264**, 69 (1997).
8. M. Olsson, R. Shine, T. Madsen, A. Gullberg, H. Tegelström, *Nature* **383**, 585 (1996).
9. D. J. Hosken, T. W. J. Garner, T. Tregenza, N. Wedell, P. I. Ward, *Proc. R. Soc. London Ser. B* **270**, 1933 (2003).
10. T. Tregenza, N. Wedell, *Nature* **415**, 71 (2002).
11. A. Burt, R. Trivers, *Genes in Conflict: The Biology of Selfish Genetic Elements* (Harvard Univ. Press, Cambridge, MA, 2006).
12. D. Haig, C. T. Bergstrom, *J. Evol. Biol.* **8**, 265 (1995).
13. T. A. R. Price, N. Wedell, *Genetica* **132**, 295 (2008).
14. J. Jaenike, *Annu. Rev. Ecol. Syst.* **32**, 25 (2001).
15. J. Powell, *Progress and Prospects in Evolutionary Biology: The Drosophila Model* (Oxford Univ. Press, Oxford, 1997).
16. S. H. Bryant, A. T. Beckenbach, G. Cobbs, *Evolution* **36**, 27 (1982).
17. D. Policansky, B. Dempsey, *Evolution* **32**, 922 (1978).
18. T. A. R. Price *et al.*, *Evolution* **62**, 1644 (2008).
19. W. Rice, B. Holland, *Evolution* **59**, 682 (2005).
20. L. D. Hurst, A. Pomiankowski, *Genetics* **128**, 841 (1991).
21. J. Jaenike, *Am. Nat.* **148**, 237 (1996).
22. F. Jiggins, G. Hurst, M. Majerus, *Am. Nat.* **154**, 481 (1999).
23. D. R. Taylor, P. K. Ingvarsson, *Genetica* **117**, 27 (2003).
24. L. W. Beukeboom, *Evol. Ecol.* **8**, 1 (1994).
25. F. E. Champion de Crespigny, N. Wedell, *Proc. R. Soc. London Ser. B* **273**, 1455 (2006).
26. T. K. Rajendra, K. V. Prasanth, S. C. Lakhota, *J. Genet.* **80**, 97 (2001).
27. Isofemale lines were collected with assistance from T. Markow. We thank J. Blount, F. E. Champion de Crespigny, D. J. Hosken, and T. Tregenza for discussion. Funded by a Natural Environment Research Council grant (N.W. and G.H.).

Supporting Online Material

www.sciencemag.org/cgi/content/full/322/5905/1241/DC1
Materials and Methods
References

25 July 2008; accepted 15 October 2008
10.1126/science.1163766

Regulation of Microtubule Dynamics by Reaction Cascades Around Chromosomes

Chaitanya A. Athale, Ana Dinarina, Maria Mora-Coral, Céline Pugieux, François Nedelec, Eric Karsenti*

During spindle assembly, chromosomes generate gradients of microtubule stabilization through a reaction-diffusion process, but how this is achieved is not well understood. We measured the spatial distribution of microtubule aster asymmetry around chromosomes by incubating centrosomes and micropatterned chromatin patches in frog egg extracts. We then screened for microtubule stabilization gradient shapes that would generate such spatial distributions with the use of computer simulations. Only a long-range, sharply decaying microtubule stabilization gradient could generate aster asymmetries fitting the experimental data. We propose a reaction-diffusion model that combines the chromosome generated Ran-guanosine triphosphate-Importin reaction network to a secondary phosphorylation network as a potential mechanism for the generation of such gradients.

In eukaryotic cells, chromosomes regulate spindle assembly by generating a gradient of Ran-guanosine triphosphate (RanGTP) in their vicinity (1–5). In frog eggs and egg extracts, it has been shown that this gradient triggers the nucleation of spindle microtubules (MTs) by activating the protein TPX2 (6) and stabilizes the plus ends of centrosomal MTs by activating the kinase CDK11

(7). When centrosomes are incubated together with chromatin stripes or beads in those extracts, the centrosomal asters are asymmetric, sending longer microtubules preferentially toward chromatin, presumably because of their increased stability in this region (8, 9). However, the exact distribution of the CDK11-dependent MT stabilization activity and how this could translate into a defined asym-

metry of centrosomal asters in the vicinity of chromosomes has remained unclear.

To visualize the shape of the stabilization gradient, we designed an experimental system allowing the precise measurement of centrosomal MT asymmetry as a function of centrosome distance from chromatin (10). We immobilized chromatin beads on patches of defined sizes and distributions and incubated them in *Xenopus* egg extracts containing purified human centrosomes (Fig. 1, A and B). The chromatin patches nucleated MTs actively, and spindles assembled robustly on practically all patches. In the experiments designed to assay aster asymmetry, we added anti-TPX2 antibodies to the extract to prevent chromatin mediated MT nucleation around the beads and their interaction with centrosome-nucleated MTs (7). In this assay, centrosomal MTs displayed a radial symmetric distribution when far away from chromatin patches and became asymmetric when closer, whereas no obvious interactions between astral microtubules and the beads could be detected (Fig. 1B).

In parallel to this experimental setup, we developed a simple generic model to carry out com-

Cell Biology and Biophysics Unit, European Molecular Biology Laboratory (EMBL), Meyerhofstrasse 1, Heidelberg, Germany.

*To whom correspondence should be addressed. E-mail: karsenti@embl.de

puter simulations. It includes a centrosome with dynamic MTs, circular chromatin, and a MT stabilization gradient (Fig. 1, C and D). The centrosome nucleates a finite number of MTs from equally spaced points on its periphery. According to the MT dynamic instability model, MTs are allowed to grow and shrink with parameter values v_g and v_s (velocities of growth and shrinkage, respectively) and f_{cat} and f_{res} (frequencies of catastrophe and rescue, respectively), derived from measurements in mitotic *Xenopus* extracts (table S1) (Fig. 1C). In the absence of a gradient, the average MT length ($\langle L \rangle$) rises rapidly and achieves a symmetric steady-state value of 4.23 μm within 100 s. This matches the value obtained from an analytical solution (4.25 μm) (11). The stabilization gradient is modeled as a two-dimensional spatial change in f_{cat} and f_{res} scaled between values measured in mitotic extracts and extracts containing RanQ69L (12) (Fig. 1D and table S1). The RanQ69L values are assumed to correspond to the situation around chromatin. For a gradient with a range of $\sim 20 \mu\text{m}$ and an aster located at 20 μm from the surface of chromatin, mean MT lengths also achieve a steady state within 100 s. These asters are, however, asymmetric and polarized toward chromatin with MT mean lengths of $\sim 7 \mu\text{m}$ toward chromatin and 5 μm away from it (Fig. 1D).

Using the experimental setup, we measured the maximal aster asymmetry (C_α) as a function of centrosome position relative to chromatin (Fig. 2A). C_α reached a maximum value (~ 2) when centrosomes were $\sim 20 \mu\text{m}$ from chromatin, in agreement with previous results (8). When centrosomes were further away (between 50 and 100 μm), C_α was close to 1 (symmetric asters). We found a linear correlation between the C_α value of each aster and the length of its longest MT pointing toward chromatin (Fig. 2B), indicating that the change in C_α was due to a lengthening of MTs toward chromatin and not to a possible shortening of MTs away from it. A few astral MTs were longer than the chromatin-centrosome distance (Fig. 2C). Although we do not rule out that they physically contact the chromatin, we can explain the MT lengthening simply by the stabilizing effects of diffusible factors generated by chromatin. Such weak asymmetries were generated by a highly stochastic process involving MT dynamic instability (movies S1 and S2).

We thus screened for f_{cat} and f_{res} gradient shapes that would generate the aster asymmetry observed experimentally. A long-range shallow gradient, a short exponential, and a long-range step gradient were tested (Fig. 2, D to F). Of these, only the step gradient with a cutoff distance of $R_c = 22 \mu\text{m}$ reproduced the asymmetry measured in the experiments (Fig. 2F). The long-range step gradient reproduced the experimental values better than any other tested model because the asymmetry is expected to be maximal at the edge of the decaying stabilization gradient. On either side of this edge, asymmetry should tend toward the minimum; i.e., $C_\alpha \sim 1$.

We then simulated the functional consequence of the astral asymmetry caused by a long-range step gradient on the first capture time (t_c) of a single microtubule by chromatin. Previous models such as random (13) or biased (14) “search and capture” have predicted biologically unreasonable t_c values ($>30 \text{ min}$) for centrosomes located farther than $\sim 30 \mu\text{m}$ from chromatin. In the presence of the step gradient described here, t_c remains on the order of a few minutes for centrosome-chromatin distances as large as 45 μm (fig. S2). In addition, the capture-time values appear less variable in the presence of a step gradient. This is consistent with the previous finding that t_c is sensitive to location of the centro-

some with respect to the edge of a sharply decaying stabilization gradient (14). Thus, long-range, abruptly decaying stabilization gradients efficiently reduce t_c and increase the robustness of the search and capture mechanism.

What kind of molecular mechanism could produce a long-range, sharp decaying gradient of f_{res} and f_{cat} values around chromatin in the cytoplasm? In developmental biology (15–17), eukaryotic cells (18), and bacteria (19), step gradients (boundaries) are modeled by zero-order (15, 20) ultrasensitive reaction networks, but other possibilities could be thought of (such as cooperativity or positive feedback) (17). In frog egg extracts, the

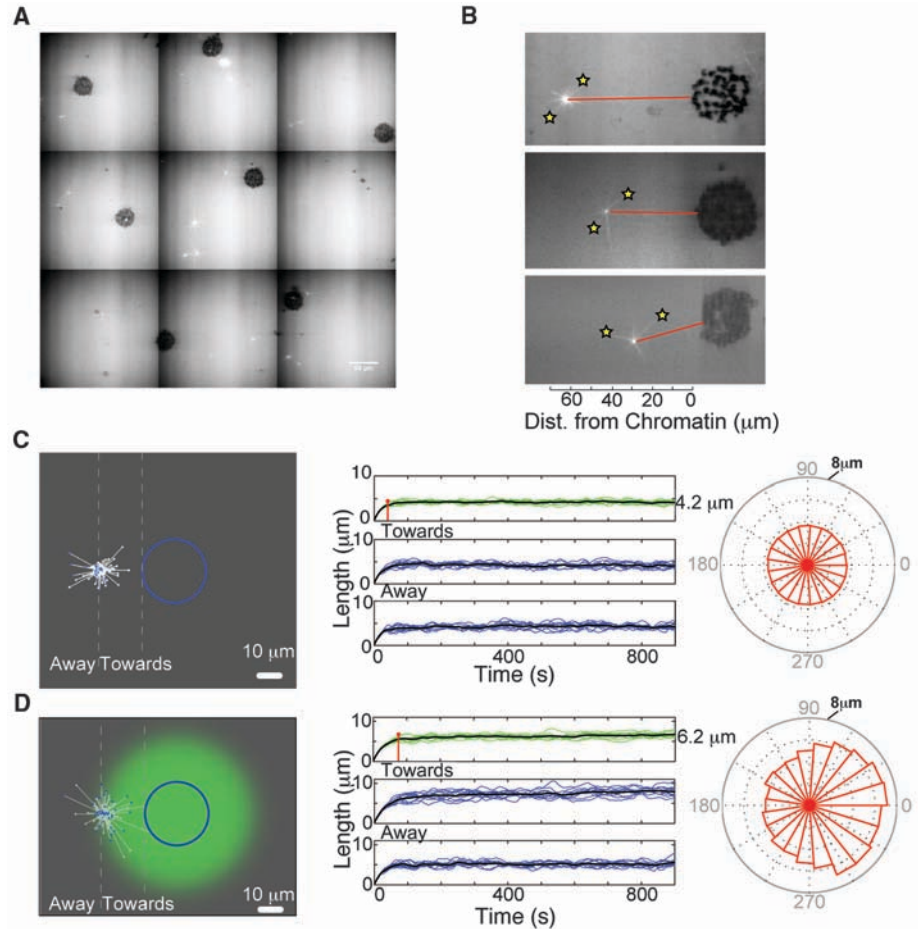


Fig. 1. Experimental and simulation of centrosomal aster asymmetry in the vicinity of chromatin. (A) *Xenopus* egg extracts with centrosomes and fluorescent tubulin were flowed into a chamber over a glass surface containing immobilized chromatin-bead patches and imaged with confocal microscopy. Centrosomes are shown in white, and the round chromatin patches are in dark gray. (B) Still images of three asters located at different distances from DNA indicate increasing asymmetry closer to the DNA surface. Stars indicate the longest microtubules in the toward and away directions, and the red line denotes the axis between the centrosome and nearest DNA patch. (C and D) Snapshot of a simulation with a centrosome near a DNA patch (blue) (C) without and (D) with the MT stabilization gradient. The f_{res} values are displayed on a scale from green to gray. The MTs ends are represented as white in a growing state and blue in a shrinking state. In the middle column, the uppermost panels indicate the MT lengths evolution in time, averaged (black lines) over 10 different runs (green lines). The two lower panels depict the time-dependent mean distribution of MT lengths pointing toward and away from the chromatin, respectively. The rightmost rose plots describe the steady-state angular distribution of the MT length (radial extent indicates length in microns) with respect to chromatin at zero degrees. The aster without a gradient is symmetric, whereas in the presence of a stabilization gradient it is asymmetric.

stabilization effect around chromosomes involves the local activation of a kinase (CDK11), which dissociates from importins in response to high RanGTP concentration (17). We therefore built a reaction-diffusion model downstream of the previously modeled Ran gradient (2), which involves a protein kinase ($E1$) and a phosphatase ($E2$) (Fig. 3A). The locally activated kinase ($E1$) converts the substrate (W) into a phosphorylated form (Wp) locally, whereas the phosphatase ($E2$), free to diffuse in the cytoplasmic space, dephosphorylates Wp globally (Fig. 3A and fig. S3). We modeled Wp as stabilizing MTs directly while W is inactive. The reaction parameters are given in table S1 and were chosen to reflect realistic kinetic constants and diffusion rates for proteins. We tested the following scenarios (Fig. 3B): (i) a linear network where $[W]$ is not saturating, (ii) a network where $WE1$ interaction is cooperative, (iii) a positive feedback network where Wp inhibits the phosphatase, and (iv) a zero-order ultrasensitive network where $[W]$ is saturating for both enzymes (15, 20). The reactions between the components are

described by the following partial differential equations

$$\frac{\partial[E1]}{\partial t} = S + (d_1 + k_1) \cdot [WE1] - a_1 \cdot [W] \cdot [E1]^n + D_1 \cdot \Delta[E1] \quad (1)$$

$$\frac{\partial[E2]}{\partial t} = (d_2 + k_2) \cdot [WpE2] - a_2 \cdot [Wp] \cdot [E2] + D_2 \cdot \Delta[E2] \quad (2)$$

$$\frac{\partial[W]}{\partial t} = -a_1 \cdot [W] \cdot [E1]^n + d_1 \cdot [WE1] + k_2 \cdot [WpE2] + D_3 \cdot \Delta[W] \quad (3)$$

$$\frac{\partial[WE1]}{\partial t} = a_1 \cdot [W] \cdot [E1]^n - (d_1 + k_1) \cdot [WE1] + D_4 \cdot \Delta[WE1] \quad (4)$$

$$\frac{\partial[Wp]}{\partial t} = -a_2 \cdot [Wp] \cdot [E2] + d_2 \cdot [WpE2] + k_1 \cdot [WE1] + D_5 \cdot \Delta[Wp] \quad (5)$$

$$\frac{\partial[WpE2]}{\partial t} = a_2 \cdot [Wp] \cdot [E2] - (d_2 + k_2) \cdot [WpE2] + D_6 \cdot \Delta[WpE2] \quad (6)$$

The term S in Eq. 1 connects this network to the RanGTP-Importin gradient-forming reaction system (supporting online material text). Also, in the above equations, d is the dissociation rate, k is the rate of product formation, a is the association rate, n is the Hill coefficient, and D is the diffusion coefficient of each species (1–6). In the positive feedback network, the parameter k_2 is replaced by a variable k'_2 , such that $k'_2 = k_2 \cdot K_f / (K_f + [Wp])$, where K_f is the feedback strength (17). Wp reaches steady-state concentration within 150 s for all models (Fig. 3C). Gradients of RanGTP and Importin- $E1$ complexes extend over 4 to 10 μm away from chromosomes with amplitudes between 0.5 and 1 μM . Gradients of $E1$, $WE1$, and $WpE2$ extend over similar distances away from chromosomes but have lower amplitudes on the order of 0.05 to 0.1 μM . Both gradient extents and amplitudes vary somewhat according to network topology. All networks generated gradients of Wp extending over 20 to 25 μm with amplitudes ranging from 0.2 to 0.8 μM , depending on the topology of the network. Only the zero order network produced a relatively long-range, sharply decaying gradient.

To examine whether some of these gradients could generate distributions of aster asymmetries as a function of chromatin distance similar to those observed experimentally, we made Wp stabilize MT plus ends by affecting MT dynamics transition frequencies as a function of chromatin distance (r) as follows

$$f_{\text{cat}}(r) = ([Wp(r)]/[Wp]^{\text{max}}) \cdot (f_{\text{cat}}^{\text{min}} - f_{\text{cat}}^{\text{max}}) + f_{\text{cat}}^{\text{max}} \quad (7)$$

$$f_{\text{res}}(r) = ([Wp(r)]/[Wp]^{\text{max}}) \cdot (f_{\text{res}}^{\text{max}} - f_{\text{res}}^{\text{min}}) + f_{\text{res}}^{\text{min}} \quad (8)$$

The gradients of MT dynamic instability parameters generated by the linear network produced an asymmetry pattern that is a poor fit to the experimental results (Fig. 4). The positive feedback network did not generate any asymmetry pattern, as expected from the shape of the Wp gradient that is too shallow (Fig. 4, A and B). The Hill cooperative and the zero-order ultrasensitive networks generated asymmetry patterns that were best fit to the experimental results, both for the amplitude and extent of the gradients (Fig. 4). The distance from chromatin at which asters showed half maximum asymmetry was on the order of 20 μm in both cases. The fit of the asymmetry generated by the ultrasensitive or Hill-cooperative networks is not as good as with the pure step gradient (compare Figs. 2C and 4B). It is possible that alternative, additional, or more complex mechanisms are at work or that we did not find the exact parameters combination. However, the present results demonstrate that it is possible to generate gradients of microtubule dynamic instability around chromosomes having

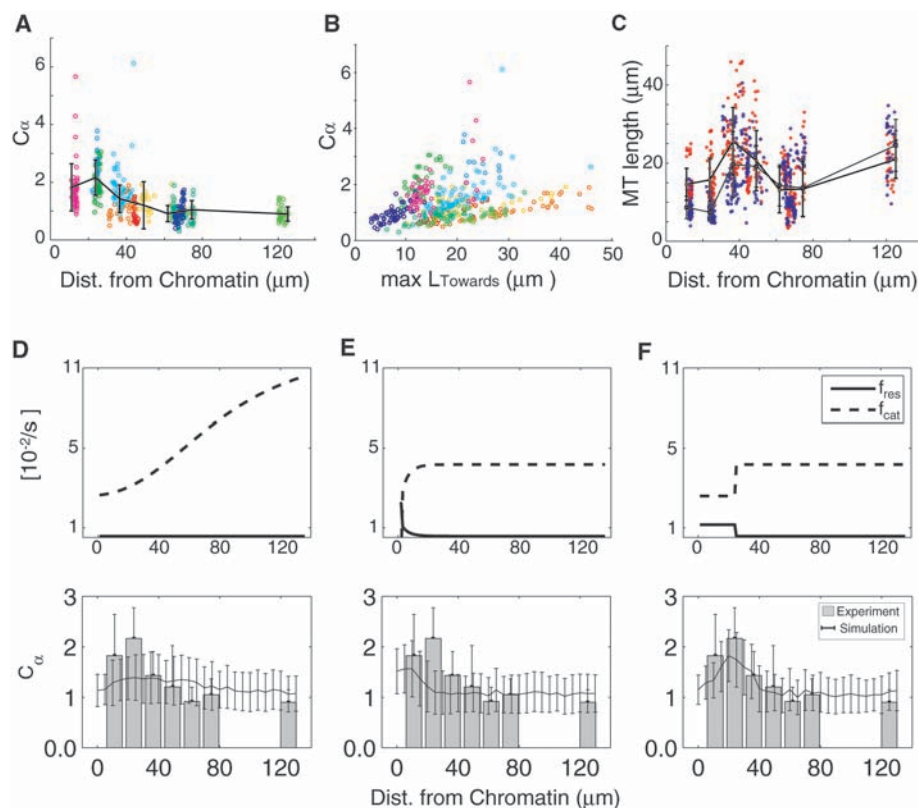


Fig. 2. Experimental measures of aster asymmetry around chromatin beads and comparison with simulations. (A) Distance of each aster from the chromatin patch in each time frame plotted against maximal asymmetry (C_α). The different colors represent individual asters, and the line plot indicates the trend of the average C_α distribution (black line) with error bars representing SD. (B) C_α plotted as a function of the length of the longest MT toward DNA. (C) Absolute lengths of MTs toward (red) and away (blue) from DNA plotted as a function of the DNA-aster distance and overlaid with mean trend lines. (D to F) f_{cat} and f_{res} values around chromatin chosen between those measured in M phase extracts and in M phase extracts treated with RanQ69L (mimicking the situation around chromatin) plotted as a long-range shallow gradient (D), a short-range exponential gradient (E), and a long-range step gradient (F). In the lower panels, the simulated C_α distributions generated by these gradients (lines) are compared with the experimental data (histograms).

an extent of $\sim 20 \mu\text{m}$ with enzymatic networks composed of proteins having realistic diffusivity and kinetic constants.

Our hypothetical network consists of a kinase-phosphatase-substrate system regulated by RanGTP. Small heterotrimeric GTP-binding

protein systems are involved in various processes, ranging from signal transduction (21) to cell polarity (22) and membrane trafficking (23). In

Fig. 3. RanGTP-based hypothetical reaction networks generate long-range gradients in the cytoplasm. **(A)** Interconversion between Ran-guanosine diphosphate (RanGDP) and RanGTP by the chromatin-bound Ran-guanine nucleotide exchange factor (RCC1) opposed by the cytoplasmic Ran-GTPase activating protein (RanGAP) generates a short-range RanGTP gradient around chromatin. RanGTP binding to Importin β releases a hypothetical cargo protein E1 (a kinase that distributes over a longer-range gradient). E1 in turn catalyzes the formation of Wp, assumed to regulate MT dynamics. The part of the network that has previously been modeled (5) is displayed in gray; the hypothesized components are in black. The parameters and initial values of the reaction are described in table S1. **(B)** Different hypothetical reaction scheme for W and Wp. **(C)** (Top) A steady state is reached in a few minutes in all models. (Bottom) Each model predicts a specific steady-state concentration profile of W and Wp (left y axis) and of E1, E2, WE1, and WpE2 (right y axis). **(D)** Comparison of the free Wp gradient shapes generated by these different network topologies.

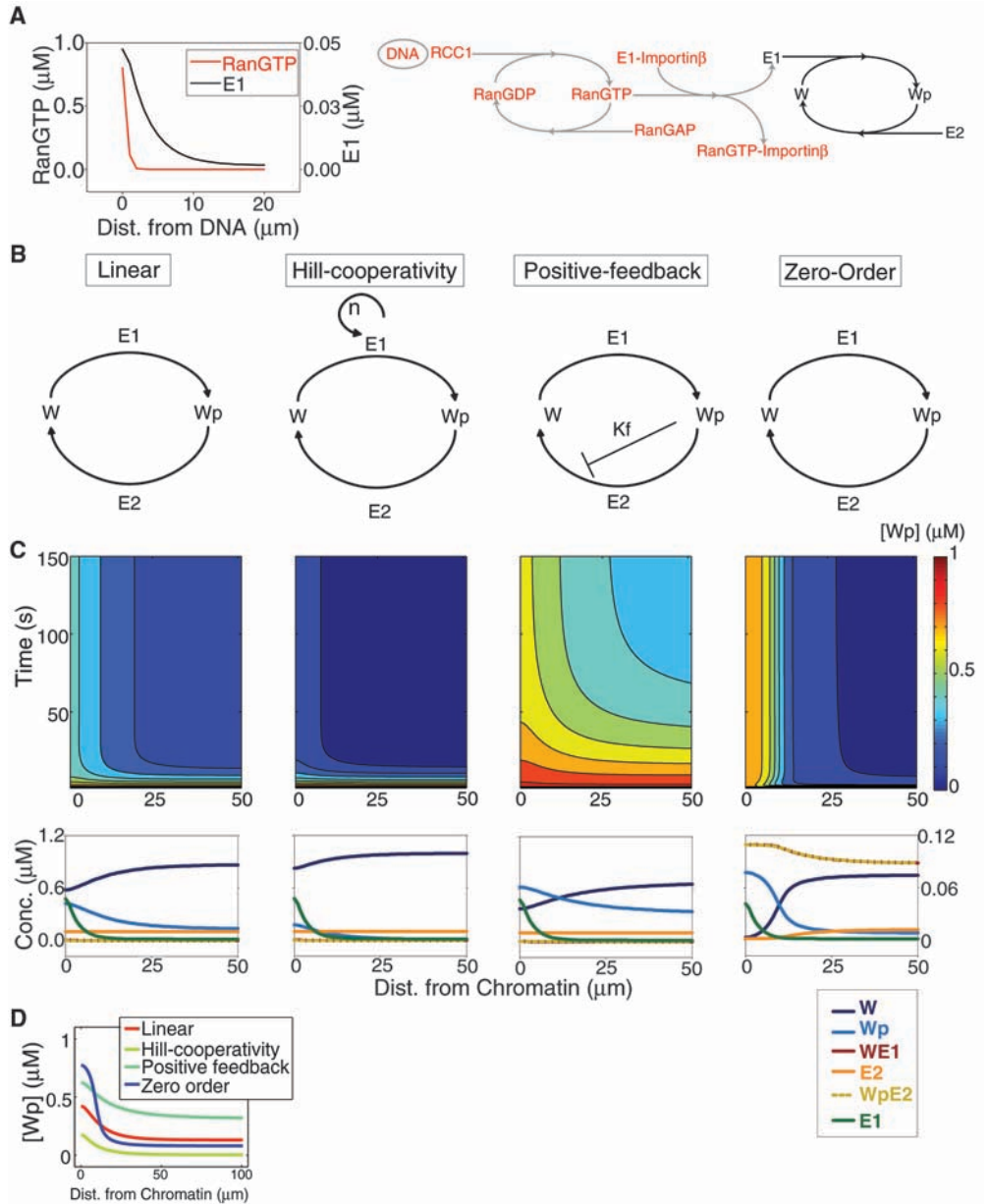
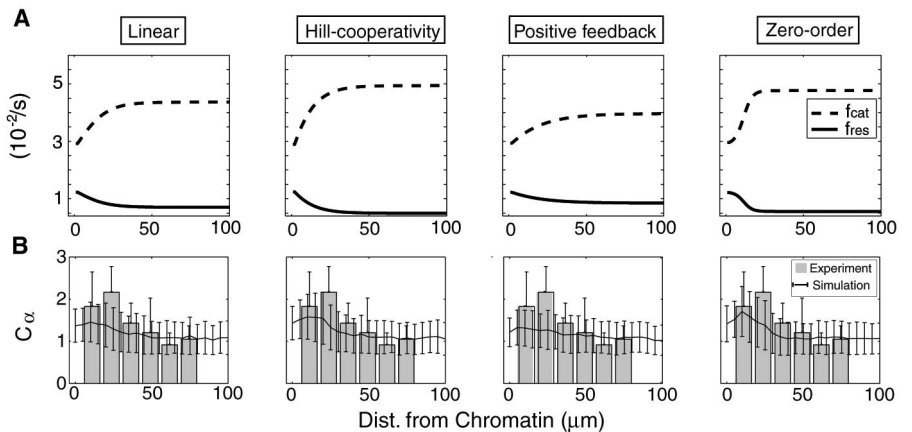


Fig. 4. The RanGTP-dependent ultrasensitive reaction-diffusion system reproduces the experimentally measured aster asymmetry. **(A)** Wp gradients obtained from the linear unsaturated, Hill-cooperative, positive feedback and zero-order ultrasensitive models are used to derive gradients of f_{cat} and f_{res} . **(B)** Simulated mean C_α obtained for the above gradients acquired for asters positioned at different distances from chromatin for the four models (lines) overlaid on the experimental data (histograms). Error bars indicate SD of the mean for both experiments and simulations. The Hill-cooperativity and zero-order ultrasensitive models fit the experimental data best.



almost all cases, they are coupled to the downstream modulation of kinase activities (24–26). Such systems may also generate local gradients involved in a variety of morphogenetic processes at the subcellular level.

References and Notes

1. P. Bastiaens, M. Caudron, P. Niethammer, E. Karsenti, *Trends Cell Biol.* **16**, 125 (2006).
2. M. Caudron, G. Bunt, P. Bastiaens, E. Karsenti, *Science* **309**, 1373 (2005).
3. P. Kalab, R. Heald, *J. Cell Sci.* **121**, 1577 (2008).
4. P. Kalab, A. Pralle, E. Y. Isacoff, R. Heald, K. Weis, *Nature* **440**, 697 (2006).
5. P. Kalab, K. Weis, R. Heald, *Science* **295**, 2452 (2002).
6. O. J. Gruss *et al.*, *Nat. Cell Biol.* **4**, 871 (2002).
7. H. Yokoyama *et al.*, *J. Cell Biol.* **180**, 867 (2008).
8. R. E. Carazo-Salas, E. Karsenti, *Curr. Biol.* **13**, 1728 (2003).
9. M. Dogterom, M. A. Felix, C. C. Guet, S. Leibler, *J. Cell Biol.* **133**, 125 (1996).
10. Materials and methods are available as supporting material on Science Online.
11. F. Verde, M. Dogterom, E. Stelzer, E. Karsenti, S. Leibler, *J. Cell Biol.* **118**, 1097 (1992).
12. R. E. Carazo-Salas, O. J. Gruss, I. W. Mattaj, E. Karsenti, *Nat. Cell Biol.* **3**, 228 (2001).
13. T. E. Holy, S. Leibler, *Proc. Natl. Acad. Sci. U.S.A.* **91**, 5682 (1994).
14. R. Wollman *et al.*, *Curr. Biol.* **15**, 828 (2005).
15. A. Goldbeter, D. E. Koshland Jr., *Proc. Natl. Acad. Sci. U.S.A.* **78**, 6840 (1981).
16. M. Howard, P. R. ten Wolde, *Phys. Rev. Lett.* **95**, 208103 (2005).
17. G. J. Meleu, S. Levy, N. Barkai, B.-Z. Shilo, *Mol. Syst. Biol.* **1**, 2005.0028 (2005).
18. J. Stelling, B. N. Kholodenko, *J. Math. Biol.*, published online 19 February 2008, 10.1007/s00285-008-0162-6.
19. S. B. van Albada, P. R. ten Wolde, *PLoS Comput. Biol.* **3**, 1925 (2007).
20. E. R. Stadman, P. B. Chock, *Proc. Natl. Acad. Sci. U.S.A.* **74**, 2761 (1977).
21. S. Etienne-Manneville, A. Hall, *Nature* **420**, 629 (2002).
22. P. G. Charest, R. A. Firtel, *Biochem. J.* **401**, 377 (2007).
23. P. Del Conte-Zerial *et al.*, *Mol. Syst. Biol.* **4**, 206 (2008).
24. V. Delorme *et al.*, *Dev. Cell* **13**, 646 (2007).
25. H. Katoh, M. Negishi, *Nature* **424**, 461 (2003).
26. C. I. Maeder *et al.*, *Nat. Cell Biol.* **9**, 1319 (2007).
27. We thank D. Foethke for inputs about the Cytosim code, M. Caudron and R. Carazo-Salas for sharing data, M. Loose for help in the initial set up of chromatin bead patterns, and the EMBL Advanced Light Microscopy Facility for invaluable help with microscopy. We acknowledge the center for Modeling and Simulation the Bioscience (BIOMS) for funding F.N. and C.A.A., the Spanish ministry of education for funding M.M.-C., European Union Specific Targeted Research Project BioMics for funding A.D., and support from Human Frontier Science Program grant RGY85.

Supporting Online Material

www.sciencemag.org/cgi/content/full/1161820/DC1

Materials and Methods

SOM Text

Figs. S1 to S4

Tables S1 and S2

References

Movies S1 and S2

16 June 2008; accepted 6 October 2008

Published online 23 October 2008;

10.1126/science.1161820

Include this information when citing this paper.

Canonical Wnt Signaling Regulates Organ-Specific Assembly and Differentiation of CNS Vasculature

Jan M. Stenman,^{1*} Jay Rajagopal,^{1,2} Thomas J. Carroll,^{1†} Makoto Ishibashi,^{1‡} Jill McMahon,¹ Andrew P. McMahon^{1,3§}

Every organ depends on blood vessels for oxygen and nutrients, but the vasculature associated with individual organs can be structurally and molecularly diverse. The central nervous system (CNS) vasculature consists of a tightly sealed endothelium that forms the blood-brain barrier, whereas blood vessels of other organs are more porous. *Wnt7a* and *Wnt7b* encode two Wnt ligands produced by the neuroepithelium of the developing CNS coincident with vascular invasion. Using genetic mouse models, we found that these ligands directly target the vascular endothelium and that the CNS uses the canonical Wnt signaling pathway to promote formation and CNS-specific differentiation of the organ's vasculature.

Several signaling pathways have been defined that generally regulate vascular development [e.g., (1)]. However, much less is known about the control of organ-specific vascularization and endothelial cell differentiation. The endothelium of the central nervous system (CNS) differs from most other organ systems in that the vascular cells establish a blood-brain barrier (BBB) that serves a critical

neuroprotective role in preventing the free flow of substances between the blood and CNS [e.g., (2)]. Consequently, the BBB also presents a physical block to the passage of potentially therapeutic agents. Diseases of the brain's vasculature are the third leading cause of death in the United States (3). Thus, defining the signaling pathways that promote the formation and differentiation of the CNS vasculature has important clinical ramifications.

At embryonic day 8.5 (E8.5) in the mouse, migrating paraxial mesoderm-derived angioblasts form a perineural vascular plexus (PNVP) surrounding the neural tube, the CNS anlagen. Endothelial cell sprouting from the PNVP initiates intraneural vascular plexus (INVP) formation at E9.5. Several Wnt family members, including *Wnt7a* and *Wnt7b*, are expressed in the neural tube coincident with neural tube angiogenesis (4). By E10.5, *Wnt7a* and *Wnt7b* are expressed in broad overlapping domains along the dorsal-ventral axis in the presumptive spinal cord and complementary patterns in the future forebrain

(fig. S1). Because single null mutants for either *Wnt7a* or *Wnt7b* (5, 6) do not exhibit an early neural tube phenotype, we derived *Wnt7a/b* double mutant embryonic stem cell lines and used tetraploid aggregations to demonstrate a neural tube-specific hemorrhaging phenotype in embryos lacking both signaling activities.

To examine the role of these Wnts in detail, we generated a more tractable genetic system in which the embryo-specific removal of *Wnt7a* and *Wnt7b* function avoided an early lethality due to *Wnt7b* function in placental development (7). In this model, all *Wnt7a/b* double mutants die around E12.5, displaying a severe CNS-specific hemorrhaging phenotype and disorganization of neural tissue (Fig. 1, A and E, and figs. S2 and S3). These data indicated that Wnt signaling is essential for CNS vascular development. In most instances, when a single active *Wnt7a* or *Wnt7b* allele remained, no phenotype was observed (figs. S2 and S3).

A detailed molecular analysis of CNS vascular development was performed using antibodies to several general endothelial markers, including fetal liver kinase 1 (FLK1) and the pericyte marker platelet-derived growth factor receptor- β (PDGFR β) (Fig. 1, B to D and F to H, and figs. S3 and S4). Consistent with normal vascular endothelial growth factor (VEGF) signaling (8), a PNVP surrounded the neural tube in *Wnt7a/b* double mutants at E12.5. However, endothelial cells and pericytes were absent from all ventral neural regions of the presumptive spinal cord except the floor plate (Fig. 1, F to H). In the dorsal neural tube, endothelial cells and pericytes were present but clustered abnormally and formed vessels with expanded lumens, most noticeably where the expression of dorsal Wnts intersects with that of *Wnt7a* and *Wnt7b* (Fig. 1F and fig. S5). Thus, whereas *Wnt7a* and *Wnt7b* are critical for ventral CNS vascularization, other Wnts may also participate in this process in more dorsal domains of the presumptive spinal cord. When

¹Department of Molecular and Cellular Biology, Harvard University, Cambridge, MA 02138, USA. ²Department of Internal Medicine, Massachusetts General Hospital, Boston, MA 02114, USA. ³Harvard Stem Cell Institute, Harvard University, Cambridge, MA 02138, USA.

*Present address: Ludwig Institute for Cancer Research, Karolinska Institute, Box 240, SE-171 77 Stockholm, Sweden.

†Present address: Department of Internal Medicine (Nephrology) and Molecular Biology, University of Texas Southwestern Medical Center, Dallas, TX 75390, USA.

‡Present address: Graduate School of Medicine, Kyoto University, Yoshida Sakyo-ku, Kyoto 606-8501, Japan.

§To whom correspondence should be addressed. E-mail: mcmahon@mcb.harvard.edu